ASME Journal of Turbomachinery
Online journal at:
https://asmedigitalcollection.asme.org/turbomachinery

A Multi-Scale Representation of Turbulence Generation in Compressor Flows

M. Dellacasagrande[1,2]
Department of Mechanical, Energy, Management and Transportation Engineering,
University of Genoa,
Genoa 16145, Italy
e-mail: matteo.dellacasagrande@edu.unige.it

P.J. Przytarski[2]
Department of Mechanical Engineering,
University of melbourne,
Melbourne, VIC 3010, Australia;
Department of Mechanical, Energy,
Management and Transport Engineering,
University of Genoa,
Genoa 16145, Italy
e-mail: pawel.przytarski@unimelb.edu.au

Turbomachinery flows exhibit strong unsteadiness, characterized by periodic wake-related disturbances superimposed on background turbulence. The turbulence generation mechanisms in these flows involve multiple interacting scales, making accurate modeling challenging. Developing robust transition models capable of capturing the multi-modal nature of these processes is crucial for accurately predicting the overall performance of turbomachinery components. In our previous work (GT2024-128738), we employed a turbulent event recognition technique that was used on high-fidelity data of a compressor cascade under steady inflow conditions to classify individual flow features as "laminar" and "turbulent" depending on their role in transition. This allowed us to characterize features such as streaks and Kelvin–Helmholtz roll-ups in a manner that is consistent and data-driven. In this work, we consider other high-fidelity scale-resolving datasets of compressor blades (NACA65) under unsteady inflow conditions. This work aims at testing whether laminar and turbulent classification is appropriate for this class of problems. For that purpose, a multi-scale analysis of the turbulence generation mechanisms is adopted. This is achieved by clustering flow scales using an unsupervised data-driven method. Following that, turbulence production for different scale clusters is examined. Data reported in the article show that a low-dimensional multi-scale representation of turbulence generation mechanisms can be achieved for compressor flows. The approach discussed here has potential to extend the concept of two-scale laminar-turbulent kinetic energy models, especially with regards to incorporating the impact of incoming wakes into the Reynolds-averaged Navier–Stokes framework. [DOI: 10.1115/1.4070237]

Keywords: compressor, LES, turbulence, multi-scale turbulence, boundary-layer development, computational fluid dynamics (CFD), fan, compressor, and turbine aerodynamic design

1 Introduction

Simulating turbomachinery flows presents significant challenges due to the multi-scale nature of velocity and pressure fluctuations. These latter can have a considerable impact on the aerodynamic performance of turbine and compressor blade profiles, see e.g., Tucker [1]. Unsteadiness arises through turbulence production mechanisms that manifest in both the boundary layer (BL) and the freestream [2]. The freestream unsteadiness provides an external forcing that contributes to the instability process within the boundary layer, providing the link between the passage and the near-wall regions.

Depending on the inflow conditions, boundary layer may transition in an attached or separated manner, affecting the overall performances of aerodynamic components, see Mayle [3]. In steady flows, small-scale freestream turbulence acts as continuous perturbation of the laminar boundary layer via the receptivity process, see e.g., Zaki [4] and Verdoya et al. [5]. For high Reynolds numbers and turbulence intensity levels, boundary layer remains attached to the blade surface. Then, the boundary-layer transitions to turbulence through a bypass-like transition process, which is dominated by the growth and breakdown of elongated streaky structures, see Jovanovic [6]. Streaks generate turbulent spots through secondary instabilities, leading to boundary-layer transition, see Zaki [4]. In contrast, at low Reynolds numbers and turbulence intensity levels such as those found in low-pressure turbines, boundary layer tends to remain laminar and may separate. If the flow subsequently reattaches to the wall, a laminar separation bubble is formed as a result, see e.g., Volino [7] and Tani [8]. The transition mechanism in such flows is typically driven by the Kelvin–Helmholtz (K–H) instability, leading to the shear layer roll-up and the generation of spanwise aligned vortices. Their breakdown finally causes the shear-layer transition and reattachment, see

Paper presented at the Turbo Expo: Turbomachinery Technical Conference & Exposition (GT2025), June 16–20, 2025.
[1]Corresponding author.
[2]Joint first authors.
Contributed by International Gas Turbine Institute (IGTI) of ASME for publication in the Journal of Turbomachinery. Manuscript received September 3, 2025; final manuscript received October 11, 2025; published online January 12, 2026. Tech. Editor: David G. Bogard.

Hosseinverdi and Fasel [9]. Several literary works have focused on developing empirical correlations for predicting transition in cases of freestream turbulence and separation-induced transition under steady flow conditions, e.g., Refs. [10–13].

In real turbomachinery flows, stochastic, small-scale background turbulence, and periodic large-scale fluctuations are present [14]. As a result, the freestream energy spectrum is strongly affected by migrating wakes when compared to a steady flow case [15]. The breakdown of the coherent large-scale fluctuations in the blade passage causes energy transfer toward smaller scales and higher frequencies in the turbulent spectrum [16]. In additions to this, the wake itself carries different turbulent scales in its core (as evidence by high turbulent kinetic energy levels within the wake) and at the interface with the surrounding freestream region, see e.g., Wissink and Rodi [17]. The impact of wake-related unsteadiness on the boundary-layer transition process can be significant, depending on the reduced frequency, the blade loading, and the wake turbulent kinetic energy levels, see e.g., Hodson et al. [18] and Wissink et al. [19]. When a laminar separation bubble forms on the blade surface, the incoming wakes can cause the periodic reattachment of the boundary layer [20], with key features of bypass and separation-induced transition occurring at different times. The unsteady flow regime therefore introduces additional spectral content into the turbulence field [17], resulting in interactions across a wider range of scales. The number of relevant scales or scale clusters to be modeled for the accurate prediction of unsteady flows therefore increases compared to a steady flow environment. Past works based on detailed experiments and high-fidelity simulations have shown how migrating wakes, boundary-layer structures, and von-Karman vortices for instance contribute differently to the overall generation of turbulence [21].

In the framework of Reynolds-averaged Navier–Stokes simulations, a two-scale representation of fluctuations in transitional boundary layers is embodied by the laminar kinetic energy (LKE) concept introduced by Walters et al. [22,23]. Large-scale coherent fluctuations forming in the laminar part of the boundary layer contribute to the production of what is called the laminar kinetic energy field. Examples are pre-transitional streaky structures in the bypass transition scenario. As the instability and breakdown of laminar structures take place, the laminar kinetic energy is transferred to the turbulent field promoting transition. In terms of modeling, an additional transport equation for LKE is required embedding an energy transfer term, which couples the laminar and turbulent kinetic energy equations.

The LKE concept originated from the observation that different flow scales have a different role in turbulence generation and transition processes [24]. While in a steady boundary-layer flow, a two-scale approach can provide an accurate representation of transition under a variety of flow scenarios [25,26], a multi-scale representation of the turbulence may represent a step forward in bridging the gap between high-fidelity methods and low-fidelity models, see e.g., Baj and Buxton [27]. In the classic LKE method, the freestream region is all classified as turbulent, regardless of the freestream turbulence spectrum. However, in unsteady turbomachinery flows, at least four spatio-temporal regions may be identified, namely the laminar and turbulent parts of the boundary layer, the periodic migrating wake, and the calm region forming in between of the successive wakes.

In this study, a turbulent event detection method is applied to highly resolved large eddy simulation (LES) data to investigate the presence of multiple scales or scale clusters in the unsteady flow-field of a compressor cascade. The analysis leverages variable spatial and temporal windowing of the data to identify such clusters. This work extends the authors' previous study [28], which focused on the steady flow data for the same compressor geometry as one analyzed here.

Table 1 Test case

Re	Ma	ϕ	F_{red}	α_{in}	F_{rotor}
140 k	0.065	1	1.71	42	273.3 Hz

2 Computational Setup

2.1 Compressor Geometry. The test case used in this study is an NACA65 compressor cascade, extensively investigated in previous works by Zaki et al. [29], Leggett et al. [30], and Przytarski and Wheeler [31]. The present compressor cascade is largely in accordance with the experiments performed by Hilgenfeld and Pfitzner [32], but lower Reynolds and Mach numbers are considered in this work. The linear cascade was denoted V103 in the experiments [32]. The current Reynolds number is $\mathrm{Re}_{C_{ax}} = 140\,\mathrm{k}$, Mach number is 0.065, and the unsteady inflow conditions are obtained with a wake-recycling procedure to produce a multi-stage like flow-field [15]. Details of the test case are shown in Table 1. The flow coefficient, and thus blade speed, is set by the stage reaction ($\Lambda = 50\%$) and the inlet and exit flow angles. The axial gap was set to $0.4C_{ax}$. Under these conditions, the suction-side (SS) boundary layer undergoes separation in between of the successive wakes, as shown in the work of Przytarski and Wheeler [15].

2.2 Solver Details. Simulations in this work were performed using the high-order compressible Navier–Stokes solver 3DNS [33]. A fourth-order DRP finite difference central scheme coupled with eighth-order standard filter was used for spatial discretization. Explicit time stepping was implemented with four-stage fractional step Runge–Kutta. Characteristic inlet and outlet boundary conditions were used to minimize the effect of reflecting pressure waves. The wake-recycling procedure, which is described in detail by Przytarski and Wheeler [15], recycles the flow from a single-passage simulation to mimic the multi-stage flow-field with a stage reaction equal to 0.5. The inflow turbulence was generated by sampling the velocity profile at a designated sampling plane and recycling it by superimposing a disturbance field onto the inflow boundary conditions at the inlet. To accurately represent the upstream rotor orientation, the tangential velocity component of the inlet disturbances was adjusted by changing its sign. Additionally, the phase of the disturbance field was varied linearly with time, effectively replicating the speed of the rotor blades.

The computational domain was discretized using a multi-block structured mesh, as shown in Fig. 1. The mesh has approximately 130M elements, with 1143k nodes in the blade-to-blade plane, and 112 nodes in the spanwise direction. The spanwise width of the domain is 10% of the axial chord and periodic boundary conditions are set in the spanwise direction. To verify the adequacy of the chosen spanwise extent, the spanwise auto-correlation function

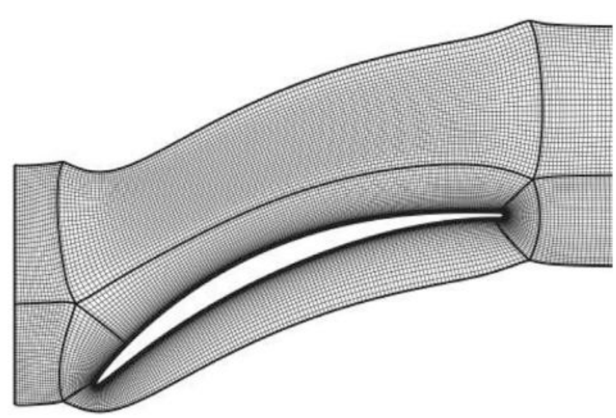

Fig. 1 Mesh used for this study showing every eighth grid line

of fluctuating velocities was computed, not shown here for brevity. The autocorrelation was seen to approach zero before the end of the domain. The wall-normal viscous wall unit (Δn^+) was set consistently lower than 1 over the entire blade surface. In the SS turbulent boundary layer, a maximum value of $\Delta n^+ = 0.6$ is obtained. The maximum tangential and spanwise viscous wall units are $\Delta t^+ = 4.8$ and $\Delta z^+ = 6$ in the SS turbulent boundary layer. These values are representative of wall-resolved LES.For the present investigation about 600 snapshots of the unsteady flow-field were collected over six rotor periods. Time-averaged statistics were computed over 20 rotor periods. The transient time covered about 15 through flows corresponding to 25 rotor periods. Further details on the methodology and the case setup can be found in the work of Przytarski and Wheeler [15].

3 Data Analysis

3.1 Scale-Cluster Identification. Simulation data in this work are used to investigate the existence of scale clusters in the unsteady flow of the NACA65 compressor cascade. To do that, a variant of a turbulent event detection method adopted in the authors' previous work [28] is used. The current method is described as follows:

(1) The sum of the absolute values of fluctuating velocity is computed for all spatial positions, namely $D = |u'| + |v'| + |w'|$, where u', v', and w' are the streamwise, wall-normal, and spanwise fluctuations, respectively
(2) Then, windowing of D is performed to evaluate this function within a small volume embedding the local fluctuations in a given range of scales. In the authors' previous work [28], a 3D spatial box was moved across the whole domain to estimate the local value of mean energy of fluctuations with maximum scale corresponding to the adopted box dimension. The 3D box dimension was chosen to match the characteristic scale of the turbulent boundary layer. In the current work, a spatio-temporal windowing is used such that it uses a subsample of data that covers a defined sub-domain and a certain number of snapshots. As a result, the windowing function is sensitive to both spatial and temporal scales of fluctuations in the unsteady flow environment
(3) Once the spatio-temporal window is defined, the root mean square (RMS) of D within the chosen window is computed and assigned to its central position (considering both spatial and temporal center points). The D RMS value is referred to as D_{RMS} for the remainder of the article. The procedure is repeated for every position as the window is moved across the whole data set. Sensitivity to the window dimension was also evaluated and is presented in the following section. Note that the local D_{RMS} value depends on both the energy and scale of fluctuations
(4) A k-means algorithm [34] is used to identify clusters of D_{RMS} values being representative of different turbulence scales and flow features. Details on the k-means procedure are given in Sec. 3.2.

3.2 k-Means Procedure. The k-means clustering method is a widely used unsupervised learning algorithm designed to partition a dataset into k distinct clusters based on feature similarity, such as the D_{RMS} values at different spatial positions and time instants. The algorithm begins by initializing k cluster centroids, which are typically chosen randomly or using an optimized seeding method, see e.g., Arthur and Vassilvitskii [35]. In this work, the first centroid is selected considering a random 10% subsample of the D_{RMS} values. The remaining centroids are selected by maximizing the probability of having the largest distance from the already chosen one [35]. This prevents initial centroids from being too close to each other and guarantees faster convergence and better clustering results compared to random initialization. Each data point is then assigned to the cluster whose centroid is the closest in terms of Euclidean distance. Once all samples are assigned to their respective class, the centroids are recalculated as the mean of the points within each cluster. This process iterates until convergence, which occurs when centroid positions no longer change or a predefined number of iterations is reached.

In this study, k-means is applied to the D_{RMS} values to identify clusters of velocity fluctuations in the unsteady compressor field. As it will be shown in Sec. 4, the probability density function (PDF) of D_{RMS} was seen to exhibit multiple peaks or modes depending on the chosen window size, which indicates the presence of underlying subpopulations or structural patterns in the data. By setting k appropriately, the k-means algorithm isolates these regions of high density of data. The clustering process allows for a data-driven segmentation that does not rely on prior assumptions about the shape or number of underlying components. The appropriate number of clusters k was indeed determined using the elbow method by plotting the within-cluster sum of squares as a function of k [36]. Once the classes are defined, each spatial position and time instant is assigned a label so that the corresponding velocity fluctuations contribute to the turbulent kinetic energy of the respective class.

3.3 Scale-Cluster Turbulent Kinetic Energy and Its Turbulence Production. For a detailed characterization of the role of scale clusters in the generation of turbulence, their contribution to the turbulent kinetic energy field (k) and its production (P_k) were compared to the overall ones. These latter are defined as follows [31]:

$$k = \sum \frac{u_{ii}'^2}{2N} \tag{1}$$

$$P_k = -\overline{u_i' u_j'} \frac{\partial U_i}{\partial x_j} \tag{2}$$

where subscripts $i, j = 1, 2, 3$ correspond to u', v', w', respectively. Upper- and lower-case letters in Eqs. (1) and (2) indicate time-mean and fluctuating velocity components, respectively. The overbar is used to indicate time-averaging of instantaneous Reynolds stresses. The comparison of P_k with the contributions from the scale clusters highlighted by the k-means procedure discussed above allowed showing the relevance of scale/energy clusters in the overall turbulence production. The turbulent kinetic energy associated to the pth class is computed as follows:

$$k_p = \sum \frac{u_{ii,p}'^2}{2N_p} \tag{3}$$

where N_p is the number of events belonging to the pth class. The corresponding time-averaged production term for a particular cluster p is defined as

$$P_{k,p} = -\overline{u_{i,p}' u_{j,p}'} \frac{\partial U_i}{\partial x_j} \tag{4}$$

The time- and spanwise-averaged values were considered to enhance statistical convergence and facilitate comparison with the overall turbulent kinetic energy and production terms.

3.4 Energy Transfer Rate Between Scale Clusters. In the two-equation LKE formulation [23], the link between laminar and turbulent kinetic energy is provided by the transfer term R that appears in both k_L and k_T equations but with opposite sign. The energy transfer rate (TR) between the pth and qth class is computed as follows:

$$\text{TR}_{q-p} = -\overline{u_{i,p}' u_{j,p}'} \frac{\partial u_{i,q}'}{\partial x_j} \tag{5}$$

4 Results

4.1 Description of Time-Mean and Instantaneous Flow-Field. Figure 2 shows the pressure and skin friction coefficients for the current test case. A small separated flow region develops from $x/C_x = 0.5$ on the blade suction side, as highlighted by the slightly negative C_f values and the change in the slope of the SS C_p distribution. As shown in the authors' work [15], boundary-layer separation is dynamically suppressed by the incoming wakes, leading to different boundary-layer states at different wake phases. Based on the C_f distribution, transition in the SS boundary layer is expected to begin at $x/C_{ax} = 0.63$ and to complete at $x/C_{ax} = 0.77$. As it will be demonstrated later in the article, different values of the D_{RMS} functions were observed in the pre-transitional, transitional, and fully turbulent part of the boundary layer, suggesting that the energy transfer among at least three different scale classes might be used to describe the transition process.

Figure 3 shows the instantaneous flow-field in the blade passage. The iso-surfaces of spanwise velocity highlight turbulent events associated with the migrating wake and the boundary-layer structures. Near the blade surface, the wall-parallel contour plot of the streamwise velocity component reveals the occurrence of streaky structures and Kelvin–Helmholtz rolls. Such flow structures are typical of the bypass and of the separation-induced transition processes. Competing transition mechanisms therefore occur in the SS boundary layer. Streaks are formed as a consequence of the wake and freestream turbulence penetrating the boundary layer [4]. When streaks propagate downstream, they perturb the separation bubble and cause the periodic suppression of the recirculating flow region. Accordingly, the region of negative C_f values shown in Fig. 2 is obtained as combination of different flow states characterized by both an attached and a separated boundary layer. In the next section, the current clustering method will be demonstrated to isolate the contribution of different flow features, as highlighted in Fig. 3, to the overall turbulent kinetic energy field.

4.2 Windowing Function Sensitivity. To evaluate the ability to capture different energy or scale clusters based on the selected spatial and temporal windowing, the function D_{RMS} was computed for a range of spatial extents of the 3D subdomain and different subsets of snapshots, as previously described. The number of snapshots used in the computation of D_{RMS} covered a temporal window ranging from 0.15 to $2T_w$, where T_w corresponds to the wake period. Similarly, the spatial window ranged approximately from 20% to 90% of the turbulent boundary-layer thickness evaluated at the SS trailing edge. These values corresponded to approximately 1.5% and 7% of the axial blade chord, respectively. Extreme cases were also considered for the sensitivity of D_{RMS} function, e.g., a case with a single spatial position or a unique time instant, i.e., single snapshot. These cases represent scenarios where only temporal or spatial windowing is applied, respectively.

Figure 4 shows probability density function distributions of the D_{RMS} values for some of the tested spatial and temporal windows. The distributions obtained from the smallest and the largest window sizes are omitted since for these cases a skewed Gaussian distribution was obtained thus preventing the possibility of identifying scale/energy clusters within the flow. Reducing the spatial/temporal window to a single point/snapshot or including the entire database also prevented identifying and localizing fluctuating events in space and time. Among the tested window sizes, a combination of a spatial window of $0.07C_{ax}$ and a temporal window of $0.3T_w$ (top row, second-column plot in Fig. 4) showed the largest number of peaks in the D_{RMS} distribution. It was determined that such spatio-temporal window will allow for the detection of the largest number of scale clusters embedded in the flow.

4.3 D_{RMS} Distribution and Scale Clusters. Figure 5 shows the probability density function of D_{RMS} values for all spatial positions and time instants obtained for the spatial and temporal window sizes of $0.07C_{ax}$ and $0.3T_w$. Three peaks resembling three Gaussian distributions can be observed with a right "fat" tail corresponding to the highest values of D_{RMS}. Accordingly, four clusters of D_{RMS} values can be identified, which correspond to four classes extracted by the k-means algorithm. It should be mentioned that the class distributions, as shown in Fig. 5, are determined by the k-means algorithm independently of the D_{RMS} PDF. Therefore, the agreement between the class distributions and the PDF peaks/bumps serves as further evidence of the capability of the present method to isolate clusters with a high density

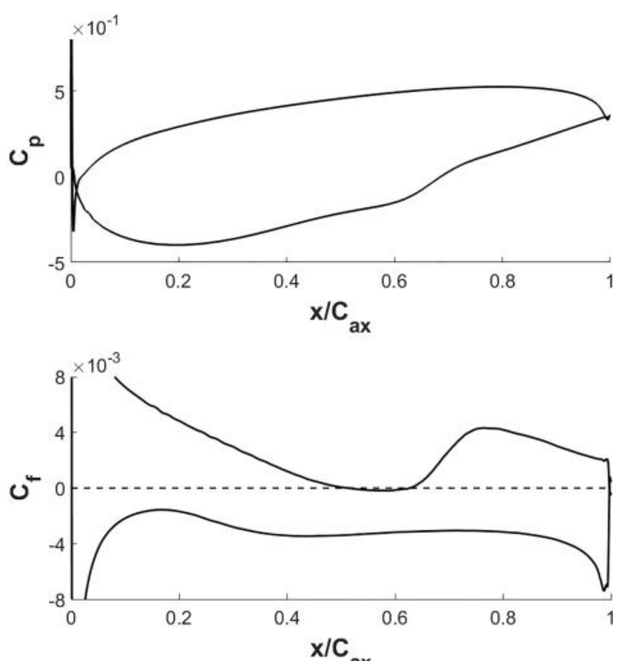

Fig. 2 Pressure (C_p) and skin friction (C_f) coefficient distributions

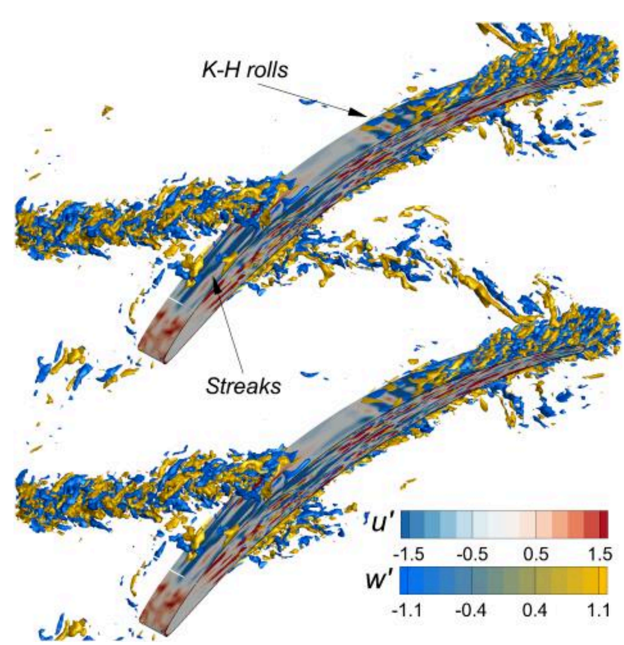

Fig. 3 Instantaneous flow-field in the compressor blade passage. Iso-surface of $w' = \pm 1.2$ and wall-parallel contour plot of u' are shown.

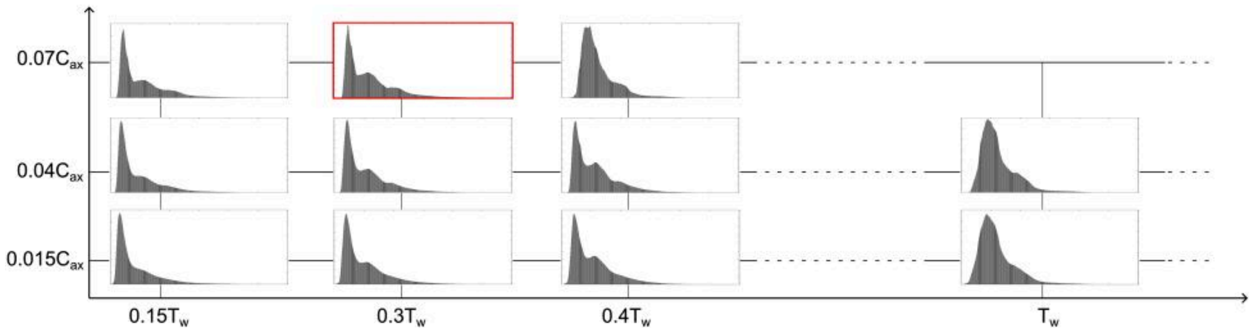

Fig. 4 Probability density function distributions of D_{RMS} for a range of spatial and temporal window sizes

of data. As shown in the following section, the classes identified through the present procedure correspond to different fluctuation scales. Therefore, they will be referred to from here on as: very small scale (VSS, Class 1), intermediate small scale (ISS, Class 2), intermediate large scale (ILS, Class 3) and very large scale (VLS, Class 4). Data corresponding to different scale clusters were grouped to compute partial kinetic energies and their corresponding turbulence production terms.

4.4 Scale-Cluster Distributions in the Unsteady Flow. Before computing the kinetic energy ascribed to each class, the spatial distribution of scale clusters is investigated. Figure 6 shows the spatial distributions of the four classes highlighted in Fig. 5. Data are shown for $t/T_w = 0, 0.25, 0.5$, and 0.75, showing the temporal variation of class distributions within the wake period. Classes named ISS, ILS, and VLS appear to describe scale/energy variation in the migrating wake and the boundary layer, while VSS class appears to correspond to the remainder of the flow-field. Several observations can be made about these class distributions. The VSS class contains freestream fluctuations as well as pre-transitional fluctuations in the fore part of the SS and pressure-side (PS) boundary layer. This class corresponds to the highest peak of D_{RMS} distribution and is characterized by the lowest D_{RMS} values, see Fig. 5. The VLS class captures the wake core as well as the largest scales in the near-wall region originating due to boundary-layer separation and its subsequent instability, i.e., the Kelvin–Helmholtz roll fluctuations. The ISS and ILS classes indicate fluctuations that transfer energy from the wake to the pre-transitional part of the boundary layer as it can be observed in the sequence of snapshots in Fig. 6 starting from $t/T_w = 0.5$. It should be noted that these latter classes persist in both the SS and PS boundary layer after the wake passage. The occurrence of the VLS class in the suction-side boundary layer seems to be triggered only by the local interaction between wake-related fluctuations and the separated boundary layer. In addition, the VLS class was never observed on the pressure side. This indicates that different scales of fluctuations characterize SS and PS boundary layer and participate in their respective transition process. This stands in contrast with a classic two-equation LKE model. The current data-driven approach

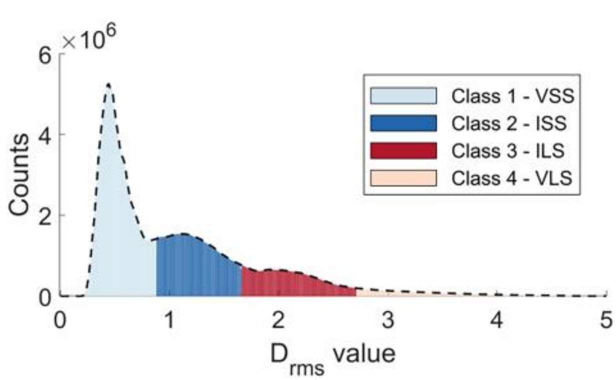

Fig. 5 Probability density function distribution of D_{RMS} for spatial and temporal window sizes equal to $0.07C_{ax}$ and $0.3T_w$

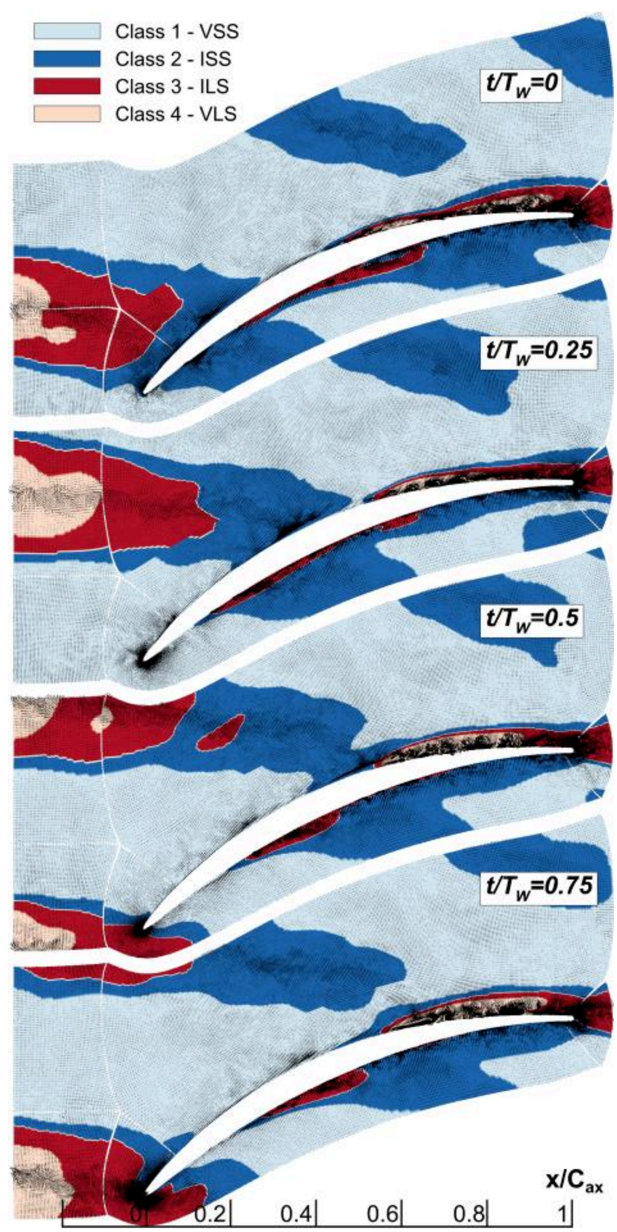

Fig. 6 Instantaneous distributions of scale clusters as determined by the k-means clustering method

may help better capture the turbulence behavior in different regions of blade cascades.

4.5 Relative Integral Values of Scale-Cluster Energy and Turbulence Production. To quantify the contribution of each scale-cluster to the total turbulent kinetic energy and the amount of turbulence production each scale-cluster is responsible for, their respective values were computed and integrated over the entire domain. Table 2 reports the relative values of k_{VSS}, k_{ISS}, k_{ILS}, and k_{VLS} and their corresponding relative turbulence production contributions. Most of the turbulent kinetic energy is retained by the ILS class, which contains the velocity fluctuations in the turbulent boundary layer, as well as those within the wake (but not strictly at the wake core). Von-Karman vortices forming at the trailing edge are also accounted by this class, as shown in Fig. 6. Large coherent fluctuations in the wake core and those linked to the Kelvin–Helmholtz instability, which are represented by the VLS class, cover approximately a quarter of the total turbulent kinetic energy. A similar amount of energy (approximately a quarter) is captured by the ISS class, which represents the fluctuations related to the wake decay and its interaction with the SS and PS boundary layers. Class named VSS on the other hand captures only 12% of the energy despite the relatively large area which it covers within the domain.

The analysis of the class-related turbulence production may provide evidence of the role that each class plays in the process of turbulence generation. This quantity depends on the combination of local level of fluctuations and shear. As expected, VSS class shows the lowest contribution to the overall turbulence production as it represents freestream fluctuations that occur in between of the successive wakes, as well as the small perturbations affecting the laminar boundary layer. Note that in a classic two-scale LKE approach, freestream fluctuations (i.e., VSS class) would be all considered as turbulent and embedded within the same class with ISS and ILS ones.

The largest quota of turbulence production is covered by the ILS and VLS classes, which are responsible for approximately 66% of total turbulence production. According to Fig. 6, ILS class captures turbulent fluctuations in the boundary layer as well as due to wake disruption and decay. On the other hand, VLS class captures the turbulence generation due to the largest scales in the wake core and in the region where the Kelvin–Helmholtz instability occurs.

4.6 Spatial Distribution of Scale-Cluster Turbulence Production Terms. Since the turbulence production strongly depends on the local strain, it follows that the contribution of each scale cluster to turbulence generation can vary significantly from one spatial location to another. Figure 7 shows the spanwise-averaged distributions of $P_{k,\mathrm{VSS}}$, $P_{k,\mathrm{ISS}}$, $P_{k,\mathrm{ILS}}$, and $P_{k,\mathrm{VLS}}$ (from top to bottom). The figure shows that most of turbulence production occurs, in a statistical sense, near the blade surface. Even if wakes are known to contribute instantaneously to the generation of turbulence [15], the averaging procedure smears the wake contribution across the domain as it occurs at different spatial positions for different time instants. It can be seen from the figure that all four classes show the negative values of turbulence production near the blade leading edge, albeit of different magnitudes. As shown by Przytarski and Wheeler [15], the negative production values observed downstream of the leading edge are due to the incoming wake. However, outside the leading edge, different distributions of turbulence productions are observed for each class, especially when comparing suction-side and pressure-side boundary layers.

Turbulence production for VSS and ISS classes shows the largest values in the fore part of the blade boundary layer, both on the suction and on the pressure sides. In addition, ISS shows high values of turbulence production (both positive and negative) on the pressure side toward the aft part of the blade. Interestingly, these two clusters relate to very different turbulence scales. The VSS class consists of primarily small-scale fluctuations representative of background turbulence, while ISS indicates scales which primarily occur at the wake interface. These classes therefore represent two distinct transition paths, one bypass and the other wake-induced. This suggests that the current data-driven procedure is able to isolate wake effects from those linked to the freestream.

Table 2 Scale-cluster contributions to partial kinetic energy and corresponding turbulence production as a fraction of the overall values

k_{VSS}	k_{ISS}	k_{ILS}	k_{VLS}
0.12	0.27	0.36	0.25
$P_{k,\mathrm{VSS}}$	$P_{k,\mathrm{ISS}}$	$P_{k,\mathrm{ILS}}$	$P_{k,\mathrm{VLS}}$
0.10	0.24	0.33	0.33

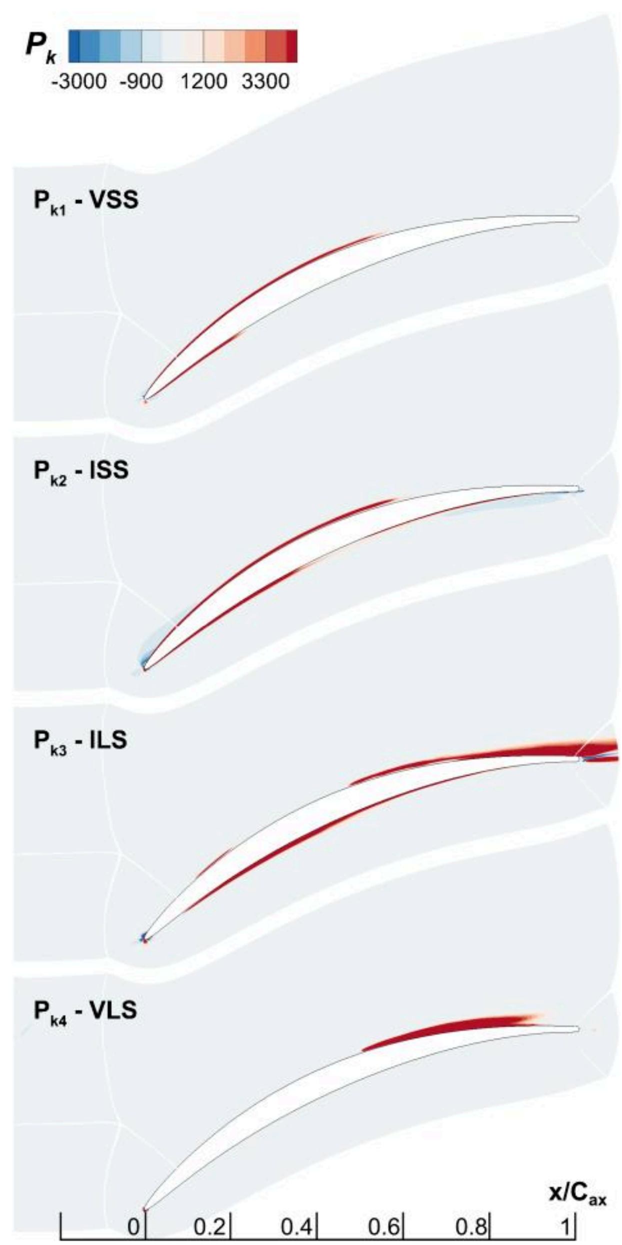

Fig. 7 Spatial distributions of P_k contributions of data-derived scale clusters. From top to bottom: VSS, ISS, ILS, and VLS classes.

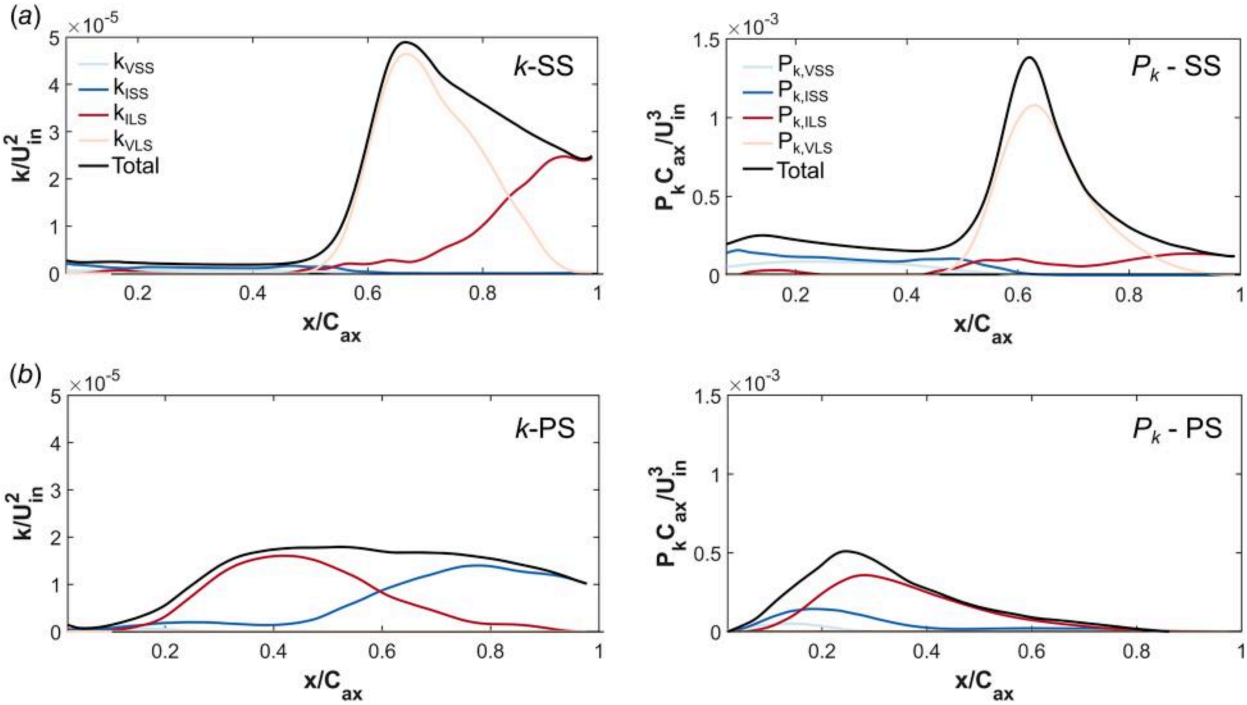

Fig. 8 Distributions of non-dimensional scale-cluster contributions to turbulent kinetic energy (k/U_{in}^2) and its production ($P_k C_{ax}/U_{in}^3$) within SS and PS boundary layers: (*a*) budgets of (left) turbulent kinetic energy and (right) its production within the SS boundary layer and (*b*) budgets of (left) turbulent kinetic energy and (right) its production within the PS boundary layer

As far as ILS class is concerned, its production represents the contribution to the overall turbulence generation due to intermediate scale structures, that occur in the outer layer of the boundary layer as well as downstream of the blade trailing edge. On the suction-side boundary layer, they seem to originate from the breakup of the Kelvin–Helmholtz rolls. On the PS, the ILS class contributes to most of turbulence generation in the front and mid sections of the blade. A bulk of production is seen to occur in the range $0.1 < x/C_{ax} < 0.4$, where wake–BL interaction was seen to occur (see e.g., Fig. 3).

Finally, the VLS class successfully captures the bulk of turbulence production due to the Kelvin–Helmholtz rolls forming as a consequence of boundary-layer separation. The region of the largest VLS production values was verified to coincide and develop from the average maximum displacement of the separation bubble. Since there is no separation bubble forming on the pressure side, VLS production is negligible in this region.

To summarize, the results presented in Fig. 7 show that the present method based on spatio-temporal windowing allows for isolating wake-related fluctuations and is able to distinguish between larger and smaller scale fluctuations driving the transition and breakdown to turbulence processes.

4.7 Budget of Scale-Cluster Turbulent Kinetic Energy and Turbulence Production in Suction-Side and Pressure-Side BoundaryLayers. Figure 8 shows the 1D budget of the partial kinetic energies and their corresponding turbulence production. Data shown in Fig. 8 are obtained by integrating scale-cluster kinetic energy and their respective turbulence production across the boundary-layer thickness both on the suction and the pressure side. These data are then scaled using the inlet freestream velocity as scaling quantity. This figure shows the evolution of all scale clusters in the shear region and therefore allows for discussing their role in transition and breakdown to turbulence processes.

4.7.1 Turbulent Kinetic Energy Within the Suction-Side Boundary Layer. The left plot in Fig. 8(*a*) shows the turbulence kinetic energy budget in the suction-side boundary layer. The figure shows that the total turbulent kinetic energy peak occurs at about $x/C_{ax} = 0.65$ which is where the transition is expected to occur based on the C_f distributions shown in Fig. 2. This peak also coincides with the peak of k_{VLS} which is linked to the occurrence of the Kelvin–Helmholtz rolls. It is clear from the figure that k_{VLS} is responsible for the majority of the energy within this peak. Downstream of that peak, k_{VLS} is seen to reduce, while k_{ILS} increases from about $x/C_{ax} = 0.6$. This indicates the transfer of energy from the large coherent rolls forming at the bubble maximum displacement to the smaller scale fluctuations occurring in the reattachment and fully turbulent regions. The overall turbulent kinetic energy remains high in the turbulent boundary layer due to the k_{ILS} contribution. Regarding the fore part of the suction side, where there is a laminar boundary layer, k_{VSS} and k_{ISS} are the dominant contributors to the local level of turbulent kinetic energy. The k_{VSS} and k_{ISS} distributions reduce to zero for the same positions at which the increment of k_{ILS} and k_{VLS} is observed. This indicates that these classes are responsible for the kinetic energy related to laminar instabilities.

4.7.2 Production of Turbulence Within the Suction-Side Boundary Layer. The right plot of Fig. 8(*a*) depicts the streamwise distribution of the contributions of each class to the overall turbulence generation in the suction-side boundary layer. The largest contributions in the pre-transitional part of the boundary layer are due to VSS and ISS classes. At these positions, the overall production term is primarily due to the sum of $P_{k,\mathrm{VSS}}$ and $P_{k,\mathrm{ISS}}$. Further downstream, $P_{k,\mathrm{ILS}}$ and $P_{k,\mathrm{VLS}}$ increase. Similarly to the turbulent kinetic energy distributions, the maximum peak of turbulence production is primarily due to the turbulence production term associated with the occurrence of separation, i.e., the VLS class. It can be also seen that the contribution of class ILS to turbulence production is reduced when compared to its contribution to the turbulence kinetic energy budget. This is consistent with the reduction of turbulence generation associated to smaller scale fluctuations in the turbulent

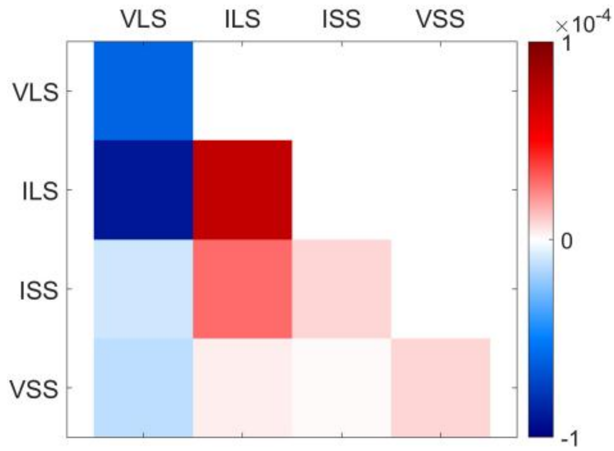

Fig. 9 Net integrated energy transfer rate between the four scale clusters

boundary layer compared to the levels typically observed near the bubble maximum height position [37].

4.7.3 Turbulent Kinetic Energy Within the Pressure-Side Boundary Layer. The left plot of Fig. 8(*b*) shows the distribution of turbulent kinetic energy in the pressure-side boundary layer. Note that the reduction of turbulent kinetic energy compared to the SS is mostly related to the disappearance of the k_{VLS} peak, which is associated with the onset of K–H vortices. This again demonstrates the capability of the present procedure to isolate the contributions of different dynamics to the turbulent kinetic energy field, which may occur at different spatial positions on the blade surface.

In the PS boundary layer, ISS and ILS classes are the main contributors to the turbulent kinetic energy field due to the formation of smaller scale fluctuations. The peak of the total turbulent kinetic energy is observed for x/C_{ax} equal to about 0.35. At the same position, the largest value of k_{ILS} is observed. Contrarily, the k_{ISS} distribution exhibits a local reduction in intensity at the position of the total kinetic energy peak. This behavior can be explained by examining the data shown in Figs. 3 and 6, where local instabilities can be observed in the PS boundary layer around $0.35x/C_{ax}$, which extend for a limited portion of the blade. Particularly, the k_{ILS} peak takes place where the wake–BL interaction on the PS was seen to occur. Further downstream, k_{ISS} increases again while k_{ILS} values reduce. The present method therefore allows for detecting localized instabilities at different streamwise locations in the boundary layer. Finally, small values of k_{VSS} are observed in fore part of the pressure side boundary layer, namely for $x/C_{ax} < 0.2$, due to the effects of impinging wakes, see e.g., Fig. 6.

4.7.4 Production of Turbulence Within the Pressure-Side Boundary Layer. As for the turbulence production terms in the pressure-side boundary layer (Fig. 8(*b*), right plot), one should note that the maximum peak of the overall turbulent kinetic energy production occurs at different streamwise locations compared to the distributions of all classes. Its location is determined mostly by the sum of the $P_{k,\mathrm{ISS}}$ and $P_{k,\mathrm{ILS}}$ contributions. Additionally, the production peak for the ISS class, i.e., for wake-related fluctuations impinging the boundary layer (see Fig. 6), does not occur at the same position for which its maximum energy value is observed. The peak in $P_{k,\mathrm{ISS}}$ occurs further upstream due to the wake and boundary-layer distortion downstream of the leading edge. This indicates that k_{ISS} fluctuations observed in the rear part of the pressure-side boundary layer are mostly generated at upstream locations and then they are convected downstream. Even though the present multi-scale representation still keeps the simplicity arising from a reduced number of scale classes, different instability mechanisms occurring in both suction- and pressure-side boundary layers can be highlighted that would be lost in a two-scale laminar-turbulent model.

4.8 Inter- and Intra-Cluster Turbulent Kinetic Energy Transfer Rate. Just as turbulence production signifies the amount of energy exchanged between the mean field and a turbulent scale-cluster, the energy transfer rate signifies the amount of energy exchanged between two different scale clusters. The mechanism of energy exchange is analogical to turbulence production and is expressed as a product of Reynolds stress tensor of scale-cluster 1 and a strain field of a scale-cluster 2. A positive value of such a transfer rate signifies that the energy flows from the scale-cluster 2 to the scale-cluster 1, i.e., scale-cluster 2 acts as an energy source and scale-cluster 1 acts as an energy sink in this exchange.

Having separated instantaneous fluctuations into distinct classes, we average them to create time-mean fields associated with each scale-cluster and compute Reynolds stresses and strains that result from them. This allows us to evaluate how scale-cluster classes interact with each other in the average sense. Given that each scale-cluster class comprises of many individual fluctuations, each class can also interact with itself. As a result there are 16 potential interactions between the previously identified four scale clusters. Twelve of these interactions correspond to the transfer of energy between different cluster classes, with each pair of classes allowing for two energy transfer pathways. We can demonstrate it using Eq. (5) by considering scale clusters VLS and ILS for which these transfer rates are as follows:

$$\mathrm{TR}_{\mathrm{VLS-ILS}} = -\overline{u'_{i,\mathrm{ILS}}u'_{j,\mathrm{ILS}}}\frac{\partial u'_{i,\mathrm{VLS}}}{\partial x_j} \tag{6a}$$

$$\mathrm{TR}_{\mathrm{ILS-VLS}} = -\overline{u'_{i,\mathrm{VLS}}u'_{j,\mathrm{VLS}}}\frac{\partial u'_{i,\mathrm{ILS}}}{\partial x_j} \tag{6b}$$

where the first interaction corresponds to the VLS class acting as an energy source and ILS acting as an energy sink with the positive value of it corresponding to the forward energy cascade (energy flowing from a very large scale to intermediate large scale); the second interaction reverses class roles with ILS acting as an energy source with the positive value corresponding to the energy back-scatter. For simplicity, we can assume the forward energy cascade as a default direction of the energy flow and sum both contributions to evaluate a net energy transfer rate from the scale VLS to ILS as such

$$R_{\mathrm{VLS-ILS}} = \mathrm{TR}_{\mathrm{VLS-ILS}} - \mathrm{TR}_{\mathrm{ILS-VLS}} \tag{7}$$

The remaining four of these interactions (out of potential 16) represent self-energy transfers where the same scale-cluster is used for both the Reynolds stress tensor term and the strain term. The energy transfer interactions between different scale clusters will be referred to as inter-cluster transfer rates while the energy transfer interactions within the same scale-cluster will be called intra-scale transfer rates.

4.8.1 Net Energy Transfer Rate. In Fig. 9, we compute and integrate these energy transfer rates across the computational domain to obtain a net energy transfer rate between each pair of scales. The resulting matrix reveals that for the majority of the scale clusters (ILS, ISS, and VSS) the dominant energy transfer rate direction is aligned with the forward energy cascade, i.e., the energy flows from the large scales to small scales. The exception from it is VLS scale-cluster for which we report negative transfer rate corresponding to energy back-scatter. We previously showed that VLS scale-cluster corresponds to the wake core and the largest scales in the near wall region originating due to boundary-layer separation. The net negative transfer rate suggests that smaller

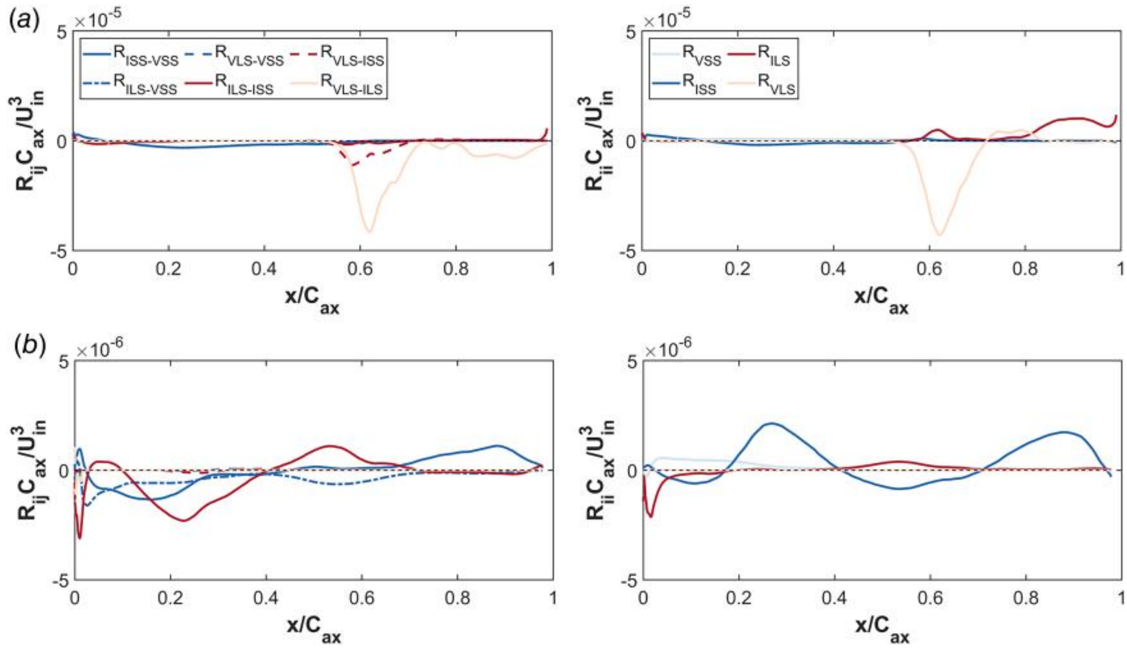

Fig. 10 Distributions of net energy transfer rate integrated across the boundary layer: (*a*) inter- (left) and intra-cluster (right) energy transfer rate in the suction-side boundary layer and (*b*) inter- (left) and intra-cluster (right) energy transfer rate in the pressure-side boundary layer

scales reinforce and strengthen large-scale fluctuations. Similar effect was previously reported by Przytarski et al. [38] using a data-driven decomposition technique based on the proper orthogonal decomposition. These authors also showed that the back-scattering effect gets stronger as the flow-field becomes more unsteady pointing to a potential feedback mechanism, i.e., high unsteadiness leads to even higher unsteadiness by energizing large-scale fluctuations.

Next we will investigate inter- and intra-cluster transfer rates within the boundary layers in order to reveal how they govern the turbulent dynamics.

4.8.2 Energy Transfer Rate Within the Suction-Side Boundary Layer. Figure 10(*a*) shows the net inter- and intra-cluster energy transfer rates integrated across the suction-side boundary layer. It is clear from the plot that the VLS scale-cluster plays a significant role in the boundary-layer behavior as it features strong negative peaks where the transition process takes place ($C_{ax} \approx 0.6$). Both inter- and intra-scale peaks relate to the energy getting transferred into larger scale structures—a back-scattering event. This is interesting from the physical standpoint as it suggests that larger Kelvin–Helmholtz rolls draw energy from the smaller scales occurring in that region. This phenomenon is supported to a varying degree by ISS, ILS, and VLS scale-cluster classes. The plots also show that in a fully developed turbulent boundary-layer region there is energy transfer from ILS class to ISS and VLS classes. This is likely related to how the periodic wake modulates the boundary layer and helps to redistribute the energy within it depending on the phase of the wake. This can be observed in Fig. 6.

4.8.3 Energy Transfer Rate Within the Pressure-Side Boundary Layer. Similarly, Fig. 10(*b*) shows the net inter- and intra-cluster energy transfer rates integrated across the pressure-side boundary layer. Here we can see significant negative energy transfer rates occurring from the leading edge to the transition location ($C_{ax} \approx 0.3$). In contrast to the suction side, the pressure-side boundary-layer transitions predominantly through a bypass transition mechanism. As such, these back-scattering events are likely related to the emergence and growth of instabilities. As a result, energy is transferred from the VSS all the way to the ILS that finally destabilize and break down to turbulence. Once the turbulent boundary-layer forms, the sign of the energy transfer rate then switches from negative to positive. This forward energy cascade is facilitated by the ILS and ISS scale clusters that channel the energy into smaller scales where it likely dissipates as manifested by the thinning of the pressure-side boundary layer toward the trailing edge.

5 Conclusion

This work investigated the possibility of extending the rationale of a two-scale classic LKE model to a multi-scale one. The initial goal was to highlight scale/energy clusters in the turbulent fields adopting a classic k-means algorithm. A turbulent events detection function was introduced that is sensitive to both the spatial and the temporal scale of fluctuations. By means of spanning different windows sizes in space and time, we highlighted the existence of four scale classes in the currently investigated compressor flow-field. These classes were associated with the background turbulence (class 1, VSS), pre-transitional fluctuations arising from wake-boundary-layer interaction (class 2, ISS), fine turbulence disturbances (class 3, ILS), and large-scale fluctuations occurring in the wake core and due to the Kelvin–Helmholtz rolls forming in case of separation (class 4, VLS). The link between the present classes and the physical phenomena occurring in the compressor cascade has been shown by means of their spatial distributions in the blade channel.

The analysis of the turbulent kinetic energy and turbulence production budgets within the boundary layers has shown the possibility of detecting localized instability processes in turbomachinery flows. Further to that, the evaluation of energy transfer rates between the identified scales shed the light on the dynamics present in the flow, thus, allowing for a more detailed characterization of the phenomena driving the transition and breakdown to turbulence. Future research will aim to understand how the scale-cluster turbulence production terms and transfer rates between these clusters can be modeled.

Acknowledgment

We acknowledge PRACE grant, which awarded access to the Fenix Infrastructure resources at CINECA, partially funded from the European Union's Horizon 2020 research and innovation program through the ICEI project under the grant agreement No. 800858. This project has received funding from the European Union Horizon 2020 research and innovation program under the Marie Sklodowska–Curie grant agreement No. 101026928 and this support is also gratefully acknowledged.

Conflict of Interest

There are no conflicts of interest.

Data Availability Statement

The datasets generated and supporting the findings of this article are obtainable from the corresponding author upon reasonable request. Data provided by a third party are listed in Acknowledgment.

Nomenclature

- k = turbulent kinetic energy
- C_f = skin friction coefficient
- C_p = pressure coefficient
- D_{RMS} = detection function of turbulent events
- P_k = production of turbulent kinetic energy
- Δn^+ = normal viscous wall unit
- Δt^+ = tangential viscous wall unit
- Δz^+ = spanwise viscous wall unit
- BCs = boundary conditions
- BL = boundary layer
- DRP = dispersion relation preserving
- FTT = flow through time
- LES = large eddy simulation
- LKE = laminar kinetic energy
- PDF = probability density function
- PS = pressure side
- RMS = root mean square
- SS = suction side

References

[1] Tucker, P. G.., 2013, "Trends in Turbomachinery Turbulence Treatments," Prog. Aerosp. Sci., **63**, pp. 1–32.
[2] Sandberg, R. D., and Michelassi, V., 2022, "Fluid Dynamics of Axial Turbomachinery: Blade-and Stage-Level Simulations and Models," Annu. Rev. Fluid Mech., **54**, pp. 255–285.
[3] Mayle, R. E., 1991, "The Role of Laminar-Turbulent Transition in Gas Turbine Engines," ASME J. Turbomach., **113**, pp. 509–537.
[4] Zaki, T. A., 2013, "From Streaks to Spots and on to Turbulence: Exploring the Dynamics of Boundary Layer Transition," Flow Turbul. Combust., **91**, pp. 451–473.
[5] Verdoya, J., Dellacasagrande, M., Barsi, D., Lengani, D., and Simoni, D., 2022, "Identification of Free-Stream and Boundary Layer Correlating Events in Free-Stream Turbulence-Induced Transition," Phys. Fluids, **34**(1), p. 014109.
[6] Jovanović, M. R., 2021, "From Bypass Transition to Flow Control and Data-Driven Turbulence Modeling: An Input–Output Viewpoint," Annu. Rev. Fluid Mech., **53**, pp. 311–345.
[7] Volino, R. J., 2002, "Separated Flow Transition Under Simulated Low-Pressure Turbine Airfoil Conditions: Part 1–Mean Flow and Turbulence Statistics," ASME Turbo Expo 2002: Power for Land, Sea, and Air, Amsterdam, The Netherlands, June, American Society of Mechanical Engineers, pp. 691–702.
[8] Tani, I., 1964, "Low-Speed Flows Involving Bubble Separations," Prog. Aerosp. Sci., **5**, pp. 70–103.
[9] Hosseinverdi, S., and Fasel, H. F., 2018, "Role of Klebanoff Modes in Active Flow Control of Separation: Direct Numerical Simulations," J Fluid Mech, **850**, pp. 954–983.
[10] Fasihfar, A., and Johnson, M. W., 1992, "An Improved Boundary Layer Transition Correlation," Turbo Expo: Power for Land, Sea, and Air, Vol. 78965, American Society of Mechanical Engineers, p. V004T09A025.
[11] Abu-Ghannam, B. J., and Shaw, R., 1980, "Natural Transition of Boundary Layers–The Effects of Turbulence, Pressure Gradient, and Flow History," J. Mech. Eng. Sci., **22**(5), pp. 213–228.
[12] Dellacasagrande, M., Lengani, D., Simoni, D., Ubaldi, M., and Zunino, P., 2020, "Evaluation of Turbulent Spot Production Rate in Boundary Layers Under Variable Pressure Gradients for Gas Turbine Applications," ASME J. Turbomach., **142**(6), p. 061003.
[13] Kubacki, S., Simoni, D., Lengani, D., Dellacasagrande, M., and Dick, E., 2021, "Extension of an Algebraic Intermittency Model for Better Prediction of Transition in Separated Layers Under Strong Free-Stream Turbulence," Int. J. Heat Fluid Flow, **92**, p. 108860.
[14] Dellacasagrande, M., Sterzinger, P. Z., Zerobin, S., Merli, F., Wiesinger, L., Peters, A., Maini, G., Heitmeir, F., and Göttlich, E., 2019, "Unsteady Flow Interactions Between a High-and Low-Pressure Turbine: Part 2—Rotor-Synchronic Averaging and Proper Orthogonal Decomposition of the Unsteady Flow Fields," Turbo Expo: Power for Land, Sea, and Air, Vol. 58554, American Society of Mechanical Engineers, p. V02AT45A011.
[15] Przytarski, P. J., and Wheeler, A. P. S., 2020, "The Effect of Gapping on Compressor Performance," ASME J. Turbomach., **142**(12), p. 121006.
[16] Johnson, P. L., 2020, "Energy Transfer From Large to Small Scales in Turbulence by Multiscale Nonlinear Strain and Vorticity Interactions," Phys. Rev. Lett., **124**(10), p. 104501.
[17] Wissink, J. G., and Rodi, W., 2006, "Direct Numerical Simulations of Transitional Flow in Turbomachinery," ASME J. Turbomach., **128**(4), pp. 668–678.
[18] Hodson, H. P., Addison, J. S., and Shepherson, C. A.., 1992, "Models for Unsteady Wake-Induced Transition in Axial Turbomachines," J. Phys. III, **2**(4), pp. 545–574.
[19] Wissink, J. G., Zaki, T. A., Rodi, W., and Durbin, P. A., 2014, "The Effect of Wake Turbulence Intensity on Transition in a Compressor Cascade," Flow Turbul. Combust., **93**, pp. 555–576.
[20] Vilmin, S., Hodson, H., Savill, A., and Dawes, W., 2003, "Predicting Wake-Passing Transition in Turbomachinery Using an Intermittency-Conditioned Modelling Approach," 33rd AIAA Fluid Dynamics Conference and Exhibit, Orlando, FL, June, p. 3995.
[21] Dellacasagrande, M., Lengani, D., Simoni, D., Ubaldi, M., Granata, A. A., Giovannini, M., Rubechini, F., and Bertini, F., 2023, "Analysis of Unsteady Loss Sensitivity to Incidence Angle Variation in Low Pressure Turbine," Turbo Expo: Power for Land, Sea, and Air, Vol. 87097, American Society of Mechanical Engineers, p. V13BT30A037.
[22] Walters, D. K., and Leylek, J. H., 2004, "A New Model for Boundary Layer Transition Using a Single-Point RANS Approach," ASME J. Turbomach., **126**(1), pp. 193–202.
[23] Walters, D. K., and Cokljat, D., 2008, "A Three-Equation Eddy-Viscosity Model for Reynolds-Averaged Navier–Stokes Simulations of Transitional Flow," ASME J. Fluid. Eng., **130**(12), p. 121401.
[24] Simoni, D., Barsi, D., Dellacasagrande, M., Lengani, D., and Yepmo, V., 2020, "Modified Formulation of Laminar Kinetic Energy Transition Models by Means of Elastic-Net of a Big Experimental Database of Separated Flows," Flow Turbul. Combust., **105**, pp. 671–697.
[25] Pacciani, R., Fang, Y., Metti, L., Marconcini, M., and Sandberg, R., 2025, "A Reformulation of the Laminar Kinetic Energy Model to Enable Multi-mode Transition Predictions," Flow Turbul. Combust., **114**, pp. 81–116.
[26] Dellacasagrande, M., Ghidoni, A., Noventa, G., and Simoni, D., 2025, "Transition Model Based on the Laminar Kinetic Energy Concept for the Prediction of All Transition Modes," Int. J. Heat Fluid Flow, **112**, p. 109680.
[27] Baj, P., and Buxton, O. R. H., 2017, "Interscale Energy Transfer in the Merger of Wakes of a Multiscale Array of Rectangular Cylinders," Phys. Rev. Fluids, **2**(11), p. 114607.
[28] Dellacasagrande, M., and Przytarski, P. J., 2024, "Turbulence Generation Mechanisms in Compressor Boundary Layers," Turbo Expo: Power for Land, Sea, and Air, Vol. 88056, American Society of Mechanical Engineers, p. V12AT29A045.
[29] Zaki, T. A., Wissink, J. G., Rodi, W., and Durbin, P. A., 2010, "Direct Numerical Simulations of Transition in a Compressor Cascade: The Influence of Free-Stream Turbulence," J. Fluid. Mech., **665**, pp. 57–98.
[30] Leggett, J., Priebe, S., Shabbir, A., Michelassi, V., Sandberg, R., and Richardson, E., 2018, "Loss Prediction in an Axial Compressor Cascade at Off-Design Incidences With Free Stream Disturbances Using Large Eddy Simulation," ASME J. Turbomach., **140**(7), p. 071005.
[31] Przytarski, P. J., and Wheeler, A. P. S., 2021, "Accurate Prediction of Loss Using High Fidelity Methods," ASME J. Turbomach., **143**(3), p. 031008.
[32] Hilgenfeld, L., and Pfitzner, M., 2004, "Unsteady Boundary Layer Development Due to Wake Passing Effects on a Highly Loaded Linear Compressor Cascade," ASME J. Turbomach., **126**(4), pp. 493–500.
[33] Wheeler, A. P. S., Dickens, A. M. J., and Miller, R. J., 2018, "The Effect of Nonequilibrium Boundary Layers on Compressor Performance," ASME J. Turbomach., **140**(10), p. 101003.
[34] Ahmed, M., Seraj, R., and Islam, S. M. S., 2020, "The K-Means Algorithm: A Comprehensive Survey and Performance Evaluation," Electronics, **9**(8), p. 1295.
[35] Arthur, D., and Vassilvitskii, S., 2006, "k-Means++: The Advantages of Careful Seeding," Technical Report, Stanford.
[36] Bholowalia, P., and Kumar, A., 2014, "EBK-Means: A Clustering Technique Based on Elbow Method and k-means in WSN," Int. J. Comput. Appl., **105**(9), pp. 17–24.
[37] Lengani, D., Simoni, D., Ubaldi, M., Zunino, P., and Bertini, F., 2017, "Analysis of the Reynolds Stress Component Production in a Laminar Separation Bubble," Int. J. Heat Fluid Flow, **64**, pp. 112–119.
[38] Przytarski, P. J., Dellacasagrande, M., Kozul, M., Agrawal, R., and Bose, S. T., 2024, "Multiscale Interactions within a Multistage Compressor," Proceedings of the 2024 Summer Program, Stanford, CA, June, Stanford University Center for Turbulence Research, pp. 415–425.